ACS APPLIED POLYMER MATERIALS

Dual Ionic Liquid-Functionalized Cellulosic Materials: Thermal, Conductive, and Morphological Properties

Elizabeth A. Hays, Gabrielle Eicher, Abneris Morales, David Salas-de la Cruz, and Kevin M. Miller*

Cite This: https://doi.org/10.1021/acsapm.3c02815 Read Online

ABSTRACT: Dual ionic liquid-substituted cellulosic materials were prepared by coupling a series of alkyne-terminated imidazoles with variable carbon spacer with azide-functionalized cellulose, followed by quaternization and anion exchange. All three of the $[NTf_2]$-bearing cellulosic materials exhibited T_g values below zero and could be cast as flexible films, which exhibited stress at break values exceeding 2.3 MPa with strain at break values up to 252%. X-ray scattering analyses indicated the amorphous nature of the cellulosic materials with three scattering peaks observed, from high-to-low q, corresponding to the amorphous halo, anion-to-anion distance, and the distance between ion aggregates, respectively. The highest degree of ionic aggregation was found to exist in the **CELL-C12-NTf$_2$** material, presumably due to the longer alkyl tethers causing more uniformity in the interaggregate spacing. The conductivity of the films was found to be on the order of 10^{-5}–10^{-6} S/cm at 30 °C. A slower increase in conductivity with temperature was observed for systems where ionic aggregation was the strongest.

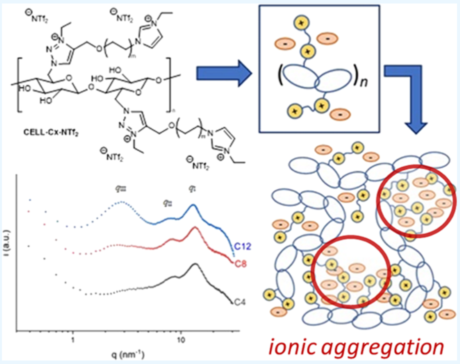

KEYWORDS: *cellulose, click chemistry, poly(ionic liquid), morphology, ionic conductivity*

■ INTRODUCTION

Materials derived from biobased, renewable sources are becoming highly sought after due to increasing concerns over environmental detriments such as global warming and plastic pollution. This concern in conservation has led to an explosion in research encompassing sustainable polymers which exhibit similar thermal and/or mechanical properties to traditional, petroleum-based materials. Polymers like cellulose, a naturally occurring polysaccharide, can offer strong mechanical properties while demonstrating sustainability, and can be utilized in the preparation of a variety of biobased monomers and functionalized biomaterials.[1−6] Cellulose is composed of glucose repeat units and is characterized by its semicrystalline fiber morphologies and high functionality.[1] Microcrystalline cellulose (MCC), a commonly used commercial derivative of cellulose, is a nanostructured material produced from an acidic hydrolysis process, which removes amorphous regions within the cellulose structure.[7] Regardless of the degree of crystallinity, cellulose can be chemically altered to adopt more favorable morphologies due to the biopolymer's multiple hydroxyl groups on each glucose unit. For example, cellulose can be acetylated, which can alter the extent of chain stiffness, cross-linking, and intermolecular interactions between the polymer chains.[1,2] Chemically modifying cellulose has led to several new applications in polymer and biomedical research as many of the resulting materials have been used in drug delivery and tissue engineering, as well as serving as optical films, and energy storage.[2,5,6,8,9]

A relatively recent method for modifying cellulose is utilizing the "click" azide−alkyne 1,3-dipolar cycloaddition strategy. The hydroxyl groups on cellulose (in particular the primary alcohol) can be converted to azides or alkyne-containing groups and then undergo cyclization to yield a substituted 1,2,3-triazole ring, typically under copper-catalyzed conditions. For example, Heinze et al. reported that 6-deoxy-6-aminopropargylcellulose could undergo click cyclization with a variety of azido-functionalized materials as indicated by nuclear magnetic resonance (NMR) and Fourier transform infrared (FTIR) spectroscopy.[10] Additional work demonstrated that highly branched polyamide dendrons could be grafted onto azide-functionalized cellulose, which in turn exhibited liquid crystalline behavior.[11] Click chemistry modifications have also been vital in research pertaining to drug discovery, synthesis of biomaterials, and cellular imaging.[11,12] Bertozzi and colleagues, for example, pioneered the use of copper-free click chemistry for dynamic *in vivo* biomolecule imaging by demonstrating that cycloaddition can occur without the toxic copper catalyst if a strained difluorocyclooctyne derivative was employed.[12] These strained derivatives were utilized to label azide-functionalized

Received: November 17, 2023
Revised: January 8, 2024
Accepted: February 1, 2024

glycans, branched carbohydrates that decorate cell membranes, on live cell surfaces. Alkyne-functionalized fibers have also been modified with azide-terminated cyclodextrins, resulting in biomaterials that exhibited antibacterial behavior against *Staphylococcus aureus*.[13]

Despite all of the groundbreaking work on functionalizing cellulose using azide−alkyne click cyclization, further quaternizing the resulting 1,2,3-triazole ring into an ionic liquid (IL), thereby creating a poly(ionic liquid) (PILs), has not been fully explored. Poly(ionic liquid)s (PILs) are a subclass of ion-containing polymers whereby an IL group is covalently attached pendant to the polymer backbone. PILs are unique in that they often retain the tunable thermal, chemical, and conductive properties of the "free" ionic liquid, but provide the benefit of mechanical stability.[14−16] As a result, PILs have been utilized in numerous applications ranging from electroactive devices to gas separation membranes.[17−20] Through altering the nature of the backbone, and ionic liquid components (cation and anion), a desired set of thermal and conductive properties can be achieved to accomplish a specific application. Ion transport in PILs relates to a number of polymer properties, including molecular weight, glass transition temperature (T_g), morphology, and ion aggregation.[21−25] Larger counterions that have a greater free volume tend to lower T_g and increase conductivity, due to an increased ability of the counteranion to "ion hop" throughout the polymer matrix or to possibly move within ion channels. Several research teams have specifically analyzed this trend, measuring ionic conductivities of a variety of counteranions, including tetrafluoroborate [BF_4], triflate [OTf], and bis(trifluoromethylsulfonyl)imide [NTf_2].[23,26,27] It was determined that, below the T_g, ionic conductivity is primarily determined by the counterion's ability to hop throughout the glassy matrix of the polymer. Temperature dependence of ionic conductivity was found to exhibit Arrhenius behavior below the T_g and changed to nonlinear behavior at temperatures above the T_g. This change can be attributed to the dependence of segmental dynamics, among other factors, which are more pertinent at temperatures above T_g. For example, several research teams have investigated the delicate interplay between polymer polarity and aggregation.[24,25] Both theory and experiment suggest that ionic aggregation is more likely if the polymer is less polar; however, aggregation may not be detrimental to ionic conductivity if the aggregates are percolated throughout the matrix rather than existing as discrete, localized clusters.

1,2,3-Triazolium-based PILs have been investigated by Drockenmuller and his team, and a review of their initial work has been published.[28] This review in part summarizes both chain-growth polymerization of 1,2,3-triazolium-containing (meth)acrylic monomers as well as the step-growth polyaddition of multifunctional azides and alkynes, leading to 1,2,3-triazolium-containing ionenes where the IL group is anchored into the backbone of the repeating unit. Drockmuller and his team have also investigated the influence of thermally reversible C−N bond transalkylations, creating vitrimeric 1,2,3-triazolium PILs and ionenes which can be reprocessed and recycled as needed.[29,30] Step-growth 1,2,3-triazolium-containing polyester networks have also been reported by our research team using a base-catalyzed carbon-Michael polymerization strategy.[31] Conductivities were found to be reasonably high (10^{-6}−10^{-8} S/cm, 25 °C, 30% RH) despite the fact that the counteranions were in a covalently cross-linked network.

As previously mentioned, reports of functionalizing cellulose with a 1,2,3-triazolium IL, or any IL (ammonium, imidazolium, phosphonium), have been few. Imidazolium-functionalized cellulose was prepared by Chen et al. by reacting chloromethylcellulose with methylimidazole, and the resulting materials were utilized as catalysts for the cycloaddition of epoxides with carbon dioxide.[32] Ammonium- and imidazolium-functionalized cellulosic materials have also been reported in carbon dioxide absorption studies.[33] More recently, Singh et al. developed a heterogeneous catalyst composed of benzimidazolium-functionalized cellulose embedded with gold nanoparticles for the purpose of reducing aromatic nitro groups to amines in water.[34] Tan and co-workers functionalized starch with 1,2,3-triazolium and pyridinium groups, and the resulting materials were found to be morphologically amorphous as determined from X-ray diffraction data.[35] The materials also exhibited antifungal activity against three different plant-threatening fungi.

Previous work in our research group has shown that MCC can be monosubstituted with 1,2,3-triazolium ILs.[36] The synthetic process included azide−alkyne click cyclization, followed by quaternization of the nitrogen on the ring to further functionalize into an ionic liquid. 1-Heptyne was used as the alkyne source, resulting in 1,2,3-triazolium IL groups with a 5-carbon alkyl "tail". The effect of counteranion on the thermal and conductive properties was analyzed utilizing [Br], [OTf], and [NTf_2]. All three 1,2,3-triazolium-functionalized cellulosic materials exhibited T_g values in the range of 90−113 °C where the larger [NTf_2] anion resulted in the lowest value. All three materials were also found to exhibit amorphous behavior, as determined from X-ray scattering experiments, and three clear scattering vectors were attributed to the amorphous halo, backbone-to-backbone distance, and the distance between neighboring ionic groups, respectively. Conductivity was over 6 orders of magnitude higher than the neutral 1,2,3-triazole derivative with a further enhancement of up to 4 orders of magnitude upon exposure to humidity (50−90%). Unfortunately, the materials were found to be mechanically very brittle, limiting the determination of mechanical properties and their general ability to be cast as membranes.

Here, we expand the scope of our initial work to MCC where each glucose unit is functionalized with two ionic liquid groups (dual-IL-functionalized cellulosic materials). Still taking advantage of the azide−alkyne click cycloaddition approach, the alkynes chosen for the present study also contain a pendant imidazole ring, thereby allowing for quaternization of both the 1,2,3-triazole and imidazole rings simultaneously, resulting in two IL groups per glucose unit [degree of substitution (DS) of 0.87−0.90]. The length of the alkyl tether between the two IL groups was varied in order to determine the breadth of thermal, mechanical, and conductive properties of the resulting derivatives. The dual-IL-functionalized route resulted in a significant decrease in the T_g (below 0 °C) as compared to the previously reported "mono-IL"-substituted cellulosic materials. Films of the dual-IL materials were found to be much more flexible and thus mechanical properties (stress−strain at break) were acquired in addition to conductivities, the latter of which were found to be on the order of 10^{-7}−10^{-6} S/cm at 30 °C. A discussion of the structure−activity relationships among the derivatives, including X-ray scattering data, is provided.

https://doi.org/10.1021/acsapm.3c02815
ACS Appl. Polym. Mater. XXXX, XXX, XXX−XXX

EXPERIMENTAL SECTION

General. All chemicals were purchased from Sigma-Aldrich or Fisher Scientific and used without further purification unless stated below. Ultrapure water, having a resistivity of 18 MΩ-cm was produced using an ELGA Purelab Ultra filtration device. ^{1}H and ^{13}C NMR spectra were acquired on a JEOL-ECS 400 MHz spectrometer, and the chemical shift values reported are referenced to residual solvent signals in either $CDCl_3$ (^{1}H, 7.26 ppm; ^{13}C, 77.36 ppm) or dimethyl sulfoxide (DMSO)-d_6 (^{1}H, 2.49 ppm; ^{13}C, 39.52 ppm). Cellulose-based samples (30 mg) were analyzed using DMSO-d_6 (0.75 mL) at 100 °C (^{1}H: 12,000 scans; ^{13}C: 50,000 scans). FTIR spectra were taken on a PerkinElmer Spectrum Two spectrometer in transmission mode, and the PerkinElmer Spectrum 10 software was used to locate and follow the desired peaks at 1 cm^{-1} resolution over 128 scans. A PerkinElmer 2400 CHNS/O Series II elemental analyzer was used to determine elemental composition (CHNS).

Synthesis of Alkynyl-Terminated Imidazoles. Described below are procedures for the **CELL-C8-NTf$_2$** analog. Analogous procedures for the **CELL-C4-NTf$_2$** and **CELL-C12-NTF$_2$** systems are provided in the Supporting Information section. Relevant NMR spectra for all derivatives are provided in the Supporting Information (Figures S1−S42).

Synthesis of Mono-THP-Protected 1,8-Octane Diol 1b. In a 500 mL round-bottom flask equipped with a magnetic stir bar, 1,8-octane diol (10.00 g, 0.0685 mol) was dissolved in dichloromethane (200 mL) with mild heating (30−35 °C). Dihydropyran (5.76 g, 0.0685 mol) was then added, followed by a catalytic (10 mg) amount of *p*-toluenesulfonic acid. The resulting solution was stirred for 24 h at room temperature, and then triethylamine was added, followed by additional stirring for 1 h. The contents were then transferred to a separatory funnel and washed with deionized (DI) water (2 × 100 mL) and brine (100 mL). The organic phase was dried over Na_2SO_4/$MgSO_4$, filtered, and the solvent was removed under reduced pressure, affording a yellow oil. The crude oil was purified by column chromatography on silica gel using a gradient elution of 0−30% ethyl acetate in hexanes. Purification resulted in 11.35 g (72%) of a clear, colorless liquid. ^{1}H NMR ($CDCl_3$): δ 4.54 (t, 1 H, J = 4.4 Hz), 3.82 (m, 1 H), 3.69 (m, 1 H), 3.60 (t, 2 H, J = 6.4 Hz, −CH_2-OH), 3.48 (m, 1 H), 3.35 (m, 1 H), 1.79 (m, 1 H), 1.68 (m, 1 H), 1.53 (m, 8 H), 1.33 (m, 8 H). ^{13}C NMR ($CDCl_3$): δ 98.84, 67.67, 62.82, 62.33, 32.78, 30.77, 29.72, 29.44, 29.39, 26.17, 25.72, 25.50, 19.66. Anal. Calcd For $C_{13}H_{26}O_3$: C 67.79, H 11.38. Found: C 67.64, H 11.06.

Synthesis of Mono-THP-Protected 1,8-Octane Diol Propargyl Ether 2b. A 100 mL round-bottom flask equipped with a magnetic stir bar under dry argon was charged with sodium hydride (2.09 g of a 60 wt % dispersion in oil, 0.0521 mol NaH) and anhydrous tetrahydrofuran (THF, 15 mL). To this stirred suspension was added dropwise a solution of **1b** (10.00 g, 0.0435 mol) in anhydrous THF (50 mL) via an addition funnel. After the addition was completed, the mixture was stirred at room temperature for 1 h, and then propargyl bromide (8.40 g of an 80 wt % solution in toluene, 0.0565 mol propargyl bromide) was added dropwise via an addition funnel. The resulting mixture was stirred at room temperature for 16 h, then quenched with saturated NH_4Cl solution (5 mL), followed by dilution with DI water (20 mL). The contents were transferred to a separatory funnel whereupon ethyl acetate (20 mL) was added. After mixing, the organic phase was isolated, washed with DI water (20 mL) and brine, (20 mL), dried over Na_2SO_4/$MgSO_4$, filtered, and the solvent was removed under reduced pressure, affording a yellow oil. Purification by column chromatography on silica gel using a gradient elution of 0−20% ethyl acetate in hexanes resulted in 8.55 g (73%) of a clear, colorless liquid. ^{1}H NMR ($CDCl_3$): δ 4.57 (t, 1 H, J = 4.0 Hz), 4.13 (d, 2 H, J = 2.4 Hz, -O-CH_2-CCH), 3.85 (m, 1 H), 3.73 (m, 1 H), 3.50 (m, 3 H), 3.38 (m, 1 H), 2.43 (t, 1 H, J = 2.4 Hz, term. alkyne), 1.83 (m, 1 H), 1.71 (m, 1 H), 1.59 (m, 8 H), 1.36 (m, 8 H). ^{13}C NMR ($CDCl_3$): δ 98.83, 80.05, 74.08, 67.64, 62.31, 58.00, 30.79, 29.74, 29.49, 29.40, 29.37, 26.18, 26.05, 25.52, 19.70. Anal. Calcd For $C_{16}H_{28}O_3$: C 71.60, H 10.52. Found: C 70.51, H 10.29.

Synthesis of 1,8-Octane Diol Monopropargyl Ether 3b. In a 250 mL round-bottom flask equipped with a magnetic stir bar, **2b** (5.78 g, 0.0216 mol) was dissolved in methanol (100 mL). Pyridinium tosylate (PPTS, 0.81 g, 3.23 mmol) was then added, followed by heating to reflux and stirring overnight. The reaction was then cooled to room temperature, and the solvent was removed under reduced pressure, affording a dark yellow oil. The crude oil was purified by column chromatography on silica gel using a gradient elution of 0−30% ethyl acetate in hexanes, resulting in 3.78 g (95%) of a clear, colorless liquid. ^{1}H NMR ($CDCl_3$): δ 4.10 (d, 2 H, J = 2.4 Hz, -O-CH_2-CCH), 3.61 (t, 2 H, J = 6.6 Hz), 3.48 (t, 2 H, J = 6.6 Hz), 2.43 (t, 1 H, J = 2.4 Hz, term. alkyne), 1.55 (m, 4 H), 1.31 (m, 8 H). ^{13}C NMR ($CDCl_3$): δ 79.95, 74.03, 70.17, 62.88, 57.93, 32.66, 29.38, 29.28, 29.25, 25.93, 25.59. Anal. Calcd For $C_{11}H_{20}O_2$: C 71.70, H 10.94. Found: C 70.61, H 10.74.

Synthesis of Tosylated 1,8-Octane Diol Propargyl Ether 4b. In a 250 mL round-bottom flask equipped with a magnetic stir bar, **3b** (3.78 g, 0.0205 mol) was dissolved in dichloromethane (45 mL). To this stirred solution were added triethylamine (6.02 g, 0.0595 mol) and catalytic *N*,*N*-dimethylaminopyridine (DMAP, 10 mg). Tosyl chloride (9.78 g, 0.0513 mol) was then added in portions over a 15 min period, followed by stirring of the resulting mixture at room temperature for 16 h. The reaction was then diluted with additional dichloromethane (200 mL) and transferred to a separatory funnel whereupon the organic phase was washed with 0.1 M HCl (100 mL) and brine (100 mL), followed by drying over Na_2SO_4/$MgSO_4$, filtration, and the solvent removal under reduced pressure. The crude dark-red oil was purified by column chromatography on silica gel using a gradient elution of 5−20% ethyl acetate in hexanes, resulting in 5.15 g (74%) of a light yellow oil. ^{1}H NMR ($CDCl_3$): δ 7.68 (d, 2 H, J = 8.4 Hz), 7.25 (d, 2 H, J = 8.4 Hz), 4.02 (d, 2 H, J = 2.4 Hz, -O-CH_2-CCH), 3.91 (t, 2 H, J = 6.4 Hz), 3.39 (t, 2 H, J = 6.6 Hz), 2.33 (s, 3 H), 2.32 (t, 1 H, J = 2.4 Hz, term. alkyne), 1.53 (m, 2 H), 1.46 (m, 2 H), 1.17 (m, 8 H). ^{13}C NMR ($CDCl_3$): δ 144.56, 133.00, 129.71, 127.74, 79.90, 74.02, 70.55, 70.02, 57.88, 29.30, 29.00, 28.68, 28.63, 25.80, 25.11, 21.52. Anal. calcd For $C_{18}H_{26}O_4S$: C 63.88, H 7.74, S 9.47. Found: C 64.37, H 7.44, S 9.31.

Synthesis of Imidazoyl 1,8-Octane Diol Propargyl Ether 5b. In a 250 mL round-bottom flask equipped with a magnetic stir bar, sodium imidazole (1.28 g, 0.0142 mol) was suspended in anhydrous THF (20 mL). A solution of **4b** (4.90 g, 0.0145 mol) in anhydrous THF (40 mL) was then added by pipet, and the resulting mixture was stirred for 1 h at room temperature, followed by 16 h at reflux. The reaction was then cooled to room temperature, filtered, and the solvent was removed from the filtrate under reduced pressure, affording a yellow oil. Column chromatography on silica gel using a gradient elution of 10−50% acetone in hexanes resulted in 2.73 g (82%) of a clear, colorless oil. ^{1}H NMR ($CDCl_3$): δ 7.55 (s, 1 H), 7.04 (s, 1 H), 6.88 (s, 1 H), 4.09 (d, 2 H, J = 2.8 Hz, -O-CH_2-CCH), 3.91 (t, 2 H, J = 7.0 Hz), 3.46 (t, 2 H, J = 6.6 Hz), 2.38 (t, 1 H, J = 2.8 Hz, term. alkyne), 1.74 (m, 2 H), 1.55 (m, 2 H), 1.32 (m, 8 H). ^{13}C NMR ($CDCl_3$): δ 136.88, 128.98, 118.67, 79.85, 73.99, 69.99, 57.87, 46.91, 30.88, 29.27, 29.02, 28.82, 26.30, 25.81. Anal. Calcd For $C_{14}H_{22}N_2O$: C 71.76, H 9.46, N 11.95. Found: C 69.94, H 9.71, N 11.55.

Synthesis of CELL-C8-TRI-IM 6b. In a 250 mL round-bottom flask with magnetic stirring, azide-functionalized MCC[36] (**CELL-N$_3$**, 1.00 g, 5.34 mmol) was dissolved in dimethyl sulfoxide (DMSO, 120 mL) at 100 °C. Once dissolved, the temperature was reduced to 70 °C and **5b** (4.20 g, 17.9 mmol) was added, followed by solutions of copper(II) sulfate (43 mg in 10 mL DI water) and sodium ascorbide (110 mg in 10 mL DI water). The resulting mixture was stirred at 70 °C for 48 h, then cooled, and precipitated onto acetone (1.5 L). The solid was isolated, broken up with a spatula, and then stirred in DI water (1.5 L) overnight. The solids were isolated, washed with acetone (200 mL), and then dried in a vacuum oven (<0.01 mmHg, 60 °C) for 48 h. Yield of a light brown solid was 1.95 g (86%) with a degree of substitution (DS) of 0.87. ^{1}H NMR (DMSO-d_6): δ 7.3−8.2 (4 H, triazole, imidazole), 3.0−5.7 (AGU repeating unit), 4.4−4.6 (2 H, tri-CH_2-O-), 3.9−4.1 (2 H, -CH_2-im), 3.3−3.4 (2 H, -O-CH_2-CH_2-

Scheme 1. Synthesis of the Alkynyl-Substituted Imidazoles 5a−c

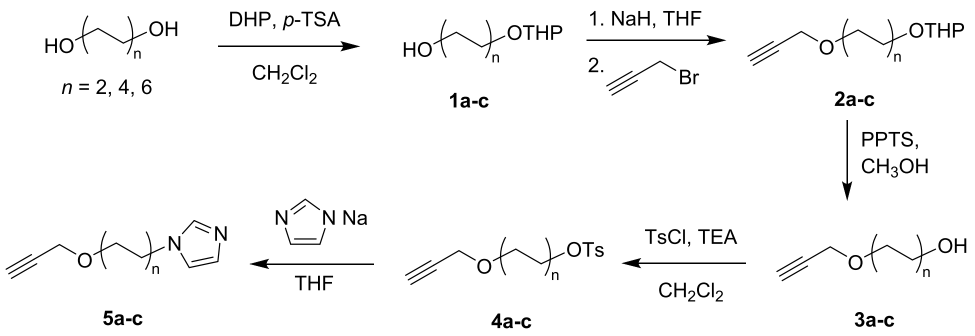

), 1.7−1.9 (2 H, -CH_2-CH_2-im), 1.4−1.6 (2 H, -O-CH_2-CH_2-), 1.0−1.3 (8 H, internal alkyl −CH_2− units). Anal. calcd For $C_{20}H_{31}N_5O_5$: C 56.99, H 7.41, N 16.62. Found: C 54.39, H 6.89, N 14.47.

Synthesis of CELL-C8-TRI-IM-Br 7b. In a poly(tetrafluoroethylene) (PTFE) screw-capped pressure vessel, **6b** (1.60 g, 3.80 mmol) was dissolved in a 10:1 solution of DMF:DMSO (50 mL total) at 100 °C. Once dissolved (16−20 h), the stirred solution was cooled to room temperature and ethyl bromide (8.27 g, 75.9 mmol) was added, followed by stirring at 60 °C for 48 h. The reaction was cooled to room temperature and precipitated onto acetone (1.5 L). The mixture was stirred for 1 h, then the solids were isolated, washed with additional acetone (2 × 250 mL), and then dried in a vacuum oven (<0.01 mmHg, 60 °C) for 48 h, resulting in 2.09 g of an off-white solid (86%) with a DS of 0.87. ^{1}H NMR (DMSO-d_6): δ 8.9−9.5 (TRI-H, IM-H^2), 7.7−7.9 (IM-H^4,H^5), 3.1−5.4 (AGU repeating unit), 4.8−4.9 (4 H, N^+-CH_2-CH_3), 4.6−4.7 (2 H, TRI-CH_2-O-), 4.1−4.2 (2 H, IM-CH_2-CH_2-), 3.5−3.6 (2 H, -O-CH_2-CH_2-), 1.8 (2 H, -CH_2-CH_2-im), 1.5−1.6 (2 H, -O-CH_2-CH_2-), 1.45 (t, 6 H, −CH_3), 1.2−1.4 (8 H, internal alkyl −CH_2− units). Anal. Calcd For $C_{24}H_{41}Br_2N_5O_5$: C 45.08, H 6.46, N 10.95. Found: C 43.38, H 6.21, N 9.54.

Synthesis of CELL-C8-TRI-IM-NTf$_2$ 8b. In a 250 mL round-bottom flask equipped with a magnetic stir bar, **7b** (1.50 g, 2.35 mmol) was dissolved in DI water (20 mL) at 60 °C. Upon dissolution, the solution was cooled to room temperature, and a solution of bis(trifluoromethane)sulfonimide lithium salt (2.02 g, 7.04 mmol) in DI water (15 mL) was added slowly by a pipet. A solid immediately formed, and the resulting solution was stirred overnight at room temperature. The solid was isolated, washed with DI water (2 × 25 mL), and dried in a vacuum oven (<0.01 mmHg, 60 °C) for 48 h, resulting in 2.15 g (89%) of a tan solid. The degree of substitution was confirmed to be 0.87 by sulfur content from elemental analysis. The degree of substitution was confirmed to be 0.87 by sulfur content from elemental analysis. ^{1}H NMR (DMSO-d_6): δ 8.8−9.1 (TRI-H, IM-H^2), 7.5−7.9 (IM-H^4,H^5), 2.8−5.3 (AGU repeating unit), 4.7−4.8 (4 H, N^+-CH_2-CH_3), 4.6 (2 H, TRI-CH_2-O-), 4.1−4.2 (2 H, IM-CH_2-CH_2-), 3.5−3.6 (2 H, -O-CH_2-CH_2-), 1.7−1.8 (2 H, -CH_2-CH_2-im), 1.6 (2 H, -O-CH_2-CH_2-), 1.4 (t, 6 H, −CH_3), 1.2−1.4 (8 H, internal alkyl −CH_2− units). Anal. Calcd For $C_{28}H_{41}F_{12}N_7O_2S_4$: C 32.34, H 3.97, N 9.43, S 12.33. Found: C 33.94, H 4.11, N 8.10, S 10.77.

Thermal Analysis. Differential scanning calorimetry (DSC) was utilized to determine any thermal transitions of the polymers at a heating rate of 2 °C/min on 3−8 mg samples. Glass transition temperatures (T_g) were determined by the inflection point of the curve observed from the second heating cycle. All DSC T_g experiments were performed in duplicate with an error of ±2.0 °C. A TA Instruments Q550 TGA (thermogravimetric analyzer) was used to evaluate $T_{d5\%}$ values (the temperature at which 5% of the material had decomposed) by heating the material under a constant nitrogen flow at a heating rate of 10 °C/min. DSC and TGA overlays for the polymers are provided in the Supporting Information (Figures S46−S51).

Film Preparation. Films of approximate thickness of 500 μm were prepared by slow evaporation of the polymer from a solution in DMF (10−15% w/w), optionally, wherein heat and/or agitation (e.g., vortexing) was applied to facilitate polymer dissolution. Once sufficient dissolution occurred to provide a homogeneous solution, it was poured into a PTFE mold assembly and allowed to dry over a period of about 24−48 h at ambient conditions, followed by 24−48 h in a 60 °C oven, then 48 h under vacuum at 60 °C. The films were then used to determine mechanical and conductive properties as described below.

Mechanical Property Analysis. A TA Instruments Q800 DMA in film tension mode with a single frequency of 1 Hz at a heating rate of 5 °C/min was utilized to determine the mechanical properties. Dynamic mechanical analysis (DMA) experiments were completed in triplicate on each sample. Tensile testing was conducted by cutting rectangular strips of each polymer samples and securing each one with the DMA film clamps. The extension, with a preload force of 0.01 N, was increased at a rate of 20 mm/min at 25 °C until each sample broke or the measurements exceeded the capabilities of the instrument.

X-ray Scattering Data. Morphological studies were conducted using a Xeuss 2.0 Dual Source Environmental X-ray scattering system. Data acquisition was performed under vacuum. A copper X-ray source was used for incident radiation, and a 1 M pixel Pilatus detector (2D) and a smaller detector were used for simultaneous small-angle (SAXS) and wide-angle X-ray scattering (WAXS) acquisition; λ = 1.54189 Å. Acquisition of data was performed for samples using full flux collimation with a 1.2 mm × 1.2 mm slit for a 600 s scan time. Using Datasqueeze 3.0, isotropic 2D scattering patterns were converted by azimuthal integration to yield a 1D profile of intensity (au) versus scattering vector q (nm^{-1}). Bragg's equation was used to calculate values for d-spacing.

Conductivity. Anhydrous ionic conductivities were measured using a TA Instruments DHR-2 discovery hybrid rheometer equipped with a dielectric accessory and a Keysight Technologies E4980AL/120 LCR meter was utilized. Each sample was dried in a vacuum oven for 48 h (60 °C, < 0.1 mmHg) for 48 h prior to analysis. The sample (approximately thickness of 500 μm) was then placed between two 25 mm stainless steel parallel-plate electrodes, and the environmental chamber was closed and kept under an atmosphere of dry nitrogen. Temperature was controlled using the environmental chamber in combination with liquid nitrogen. Dielectric permittivity and conductivity were measured isothermally over a frequency range of 20.0−10^6 Hz in 10 °C steps with an ac amplitude of ±0.01 V. Samples were kept at a constant axial force (5.0 ± 0.2 N) and soaked at each temperature for 45 min prior to obtaining measurements. The DC conductivity (σ_{DC}) was determined from the plateau value observed in the spectral dependence of the conductivity function ($\sigma' = \omega\varepsilon''\varepsilon_o$, where ω is the frequency, ε'' is the dielectric loss, and ε_o is the vacuum permittivity).

RESULTS AND DISCUSSION

In order to covalently bond the dual-IL system to the backbone of cellulose, azide−alkyne click cycloaddition chemistry was employed whereby a series of three different alkynyl-substituted imidazoles were reacted with azide-functionalized cellulose (**CELL-N$_3$**), the latter of which was

Scheme 2. Synthesis on CELL-Cx-NTf_2 Cellulosic Materials

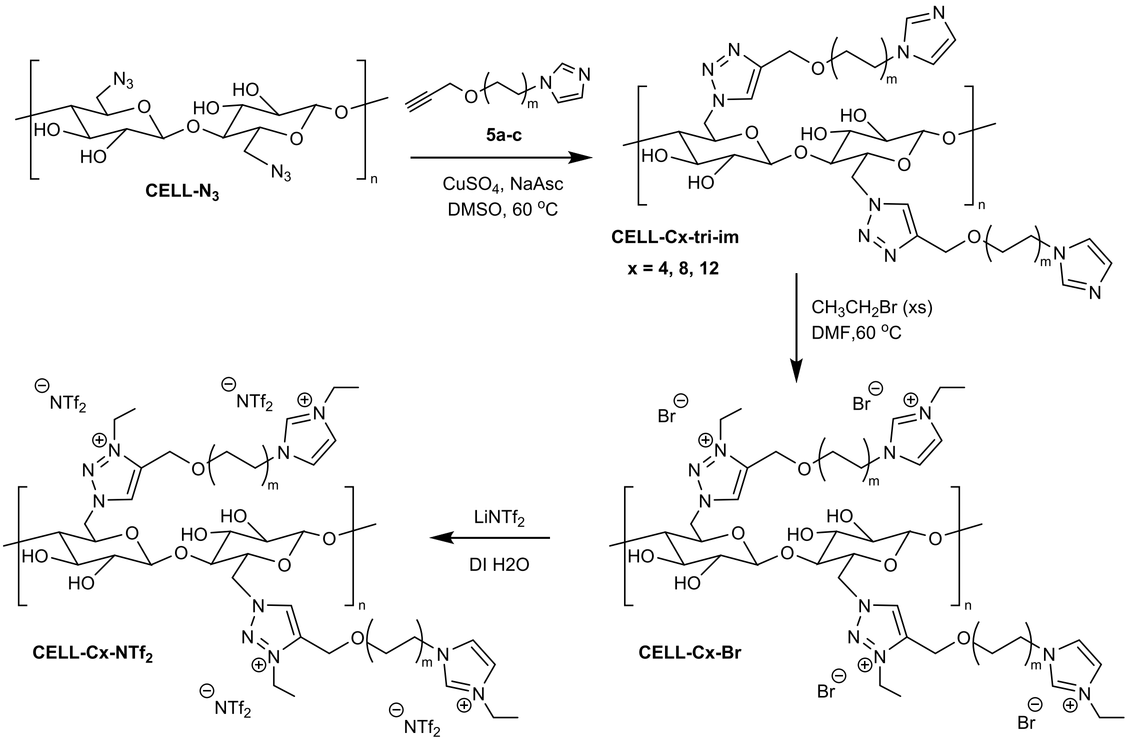

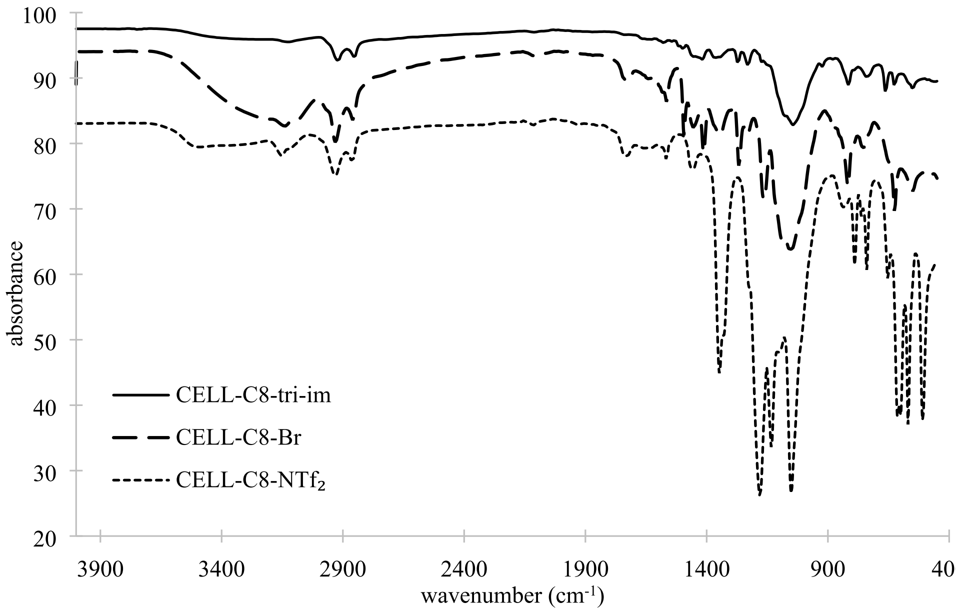

Figure 1. Overlay of FTIR spectra for the **CELL-C8** series of cellulosic materials. Overlays for the other two series can be found in the Supporting Information (Figures S44 and S45).

produced from MCC following a previously published procedure.[36] The degree of substitution (DS) of **CELL-N_3** was 0.95 as determined from elemental analysis (nitrogen content). The alkynyl-substituted imidazoles were prepared as follows. Appropriate glycol (Scheme 1; n = 2,4,6) monoprotection with dihydropyran (DHP) under acidic conditions was conducted, resulting in **1**. A Williamson ether synthesis was then conducted with sodium hydride followed by reaction with propargyl bromide providing **2**. Deprotection of the THP group occurred using PPTS (pyridinium *p*-toluenesulfonate) in refluxing methanol, producing **3**, followed by conversion to tosylates **4** using tosyl chloride under basic conditions. Finally, substitution with sodium imidazole resulted in imidazoles **5**. All of the propargyl-functionalized imidazoles were isolated as clear, colorless oils and were characterized by ^1H and ^{13}C NMR spectroscopy (Figures S1−S42) as well as elemental analysis.

Once the structure and purity of the alkynyl-substituted imidazoles **5a−c** were confirmed by NMR spectroscopy and elemental analysis, copper-catalyzed azide−alkyne click cyclization with **CELL-N_3** was undertaken with each of the propargyl-substituted imidazoles, resulting in a series of cellulosic materials termed **CELL-Cx-tri-im**, where "x" is the number of carbons of the alkyl chain between the imidazole and the ether oxygen (Scheme 2). Quaternization of both the 1,2,3-triazole and imidazole rings was then accomplished simultaneously by reacting **CELL-Cx-tri-im** with an excess of ethyl bromide in DMF in a high-pressure vessel, resulting in bromide salts **CELL-Cx-Br**. Anion exchange was completed with lithium bis(trifluoromethylsulfonyl)imide under aqueous conditions, providing the targeted **CELL-Cx-NTf$_2$** as a series of light tan solids. The DS of the **CELL-Cx-NTf$_2$** materials ranged from 0.87 to 0.90 as determined by elemental analysis (sulfur content).

Substituted cellulosic materials were characterized by NMR and IR spectroscopy, as well as elemental analysis. Confirmation of successful click cyclization was determined from the near-quantitative loss of the azide signal at 2110 cm^{-1} in the FTIR spectrum (see Figure S43 for reference) coupled with the appearance of the aromatic 1,2,3-triazole and imidazole signals in the 7−8.5 ppm range in the ^{1}H NMR spectra (for example, refer to Figure S25). Additionally, a new C=C stretching frequency at ~1550 cm^{-1} appeared (Figure 1 shows the IR spectra for the **CELL-C8** series). As all of the azide had been consumed, the nitrogen content found for the **CELL-Cx-tri-im** series was assumed to come from the two heterocycles, resulting in a DS of 0.87−0.92. Quaternization of **CELL-CX-tri-im** with ethyl bromide resulted in a shift of the aromatic proton signals downfield to 8−9.5 ppm, indicative of the triazolium and imidazolium "ionic liquid" rings. Exchange to the NTf$_2$ anion revealed a quartet in the ^{13}C NMR spectra indicative of the $-CF_3$ group (~120 ppm), and new signals at 1344, 1130, and 602 cm^{-1} (SO_2), 738 and 650 cm^{-1} (S−N−S), and 790 cm^{-1} (C−S) in the IR spectra, all of which are characteristic of the NTf$_2$ anion. Elemental analysis indicated that DS after anion exchange was 0.87−0.90 across all of the final derivatives as determined from sulfur content.

Thermal analysis of the dual-IL-functionalized cellulosic material was accomplished using DSC and TGA (Table 1). All graphical data is included in the Supporting Information. For reference, data for MCC and our previously reported mono-IL functionalized cellulose are provided. While **CELL-C12-tri-im** did not exhibit any thermal DSC transitions, subtle T_g values were found for the C4 and C8 analogues and indicated that the slightly longer C8 chain led to a small plasticization effect (i.e., T_g depression). Quaternization of the rings resulted in T_g values for all three materials and a general decrease in T_g from the nonquaternized derivatives. **CELL-C4-Br** was found to exhibit a T_g value of 69.3 °C, and a lengthening of the alkyl tether to C8 lowered the T_g to 37.1 °C; however, further lengthening to C12 resulted in an increase in T_g to 67.3 °C. While the initial decrease in T_g could be due to plasticization, the upturn in T_g from C8 to C12 is attributed to an increase in ionic and van der Waals interactions as these longer side chains begin to intercalate between different cellulose backbones, a hypothesis that will be revisited later. The trend in T_g across different alkyl tethers remained the same upon anion exchange; however, an overall decrease in values was observed due to the plasticization ability of the larger, bulkier, hydrophobic anion. This relationship between counteranion and T_g mirrors our prior work with mono-IL-substituted cellulosic materials;[36] however, the dual-IL-functionalized cellulosic materials exhibited lower T_g values as the longer chains, coupled with the imidazolium group at the end of the tether, acts to plasticize the system, further breaking up any hydrogen bonding between cellulose backbones.

Table 1. Thermal Properties of Dual-IL-Functionalized Cellulosic Materials

material	DSC T_g (°C)	TGA $T_{d5\%}$ (°C)
MCC	N/A	301
CELL-TRI-NTf$_2$ (mono)	90	240
CELL-C4-tri-im	118.5	225
CELL-C8-tri-im	74.9	226
CELL-C12-tri-im	ND	201
CELL-C4-Br	69.3	188
CELL-C8-Br	37.1	181
CELL-C12-Br	67.3	183
CELL-C4-NTf$_2$	−6.1	235
CELL-C8-NTf$_2$	−14.2	228
CELL-C12-NTf$_2$	−8.5	230

Cyclization of **CELL-N$_3$** led to a noticeable decrease in thermal stability ($T_{d5\%}$) compared to the starting microcrystalline cellulose. Additional quaternization of the rings led to another decrease in $T_{d5\%}$ value. By quaternizing the ring, a natural retro-S$_N$2 (reverse Menshutkin) decomposition pathway is introduced.[37] This coupled with a more Lewis basic anion such as bromide resulted in stability only up to ~180 °C. Anion exchange to the less-Lewis basic NTf$_2$ anion improved the thermal stability by approximately 40−50 °C. The thermal stability of the dual-IL systems was found to be very similar to the mono-IL-functionalized analog.

To evaluate mechanical and conductive properties, films with a thickness of 500 μm and a diameter of 25 mm of each of the respective **CELL-CX-NTf$_2$** materials were prepared by solvent casting from DMF into a PTFE mold of the appropriate size, resulting in a series of clear, flexible films with light to moderate brown color. The bromide versions of these materials were not evaluated as it was assumed that their conductivity would be lower based on our previously published work.[36] Films were initially evaluated by FTIR and NMR spectroscopies to ensure that no DMF solvent remained. Mechanical properties were determined using DMA (dynamic mechanical analysis). Stress−strain analysis of the films (Figure 2) indicated that **CELL-C4-NTf$_2$** exhibited the highest stress at break (2.69 ± 0.19 MPa) but the lowest elongation (133 ± 15%). Increasing the alkyl chain length led to an increase in flexibility and elongation (up to 252%) with only a small

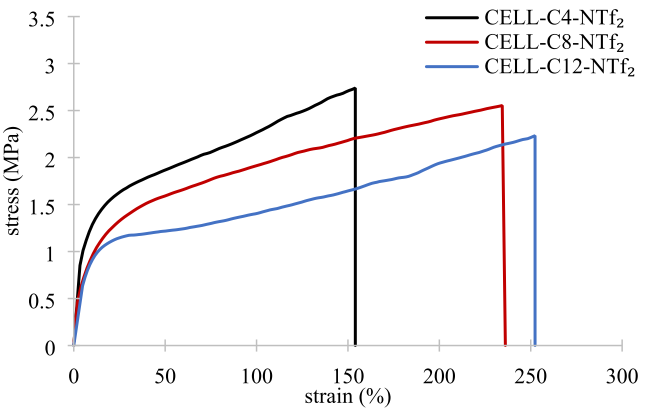

Figure 2. Overlay of representative stress−strain curves for each of the dual-IL functionalized cellulosic materials.

Table 2. Mechanical (Stress and Strain at Break) and X-ray Scattering Data for CELL-Cx-NTf$_2$ Cellulosic Materials[a]

			q_{I} (nm^{-1})	q_{II} (nm^{-1})	q_{III} (nm^{-1})
material	stress at break (MPa)	strain at break	d_{I} (nm)	d_{II} (nm)	d_{III} (nm)
CELL-C4-NTf$_2$	2.69 ± 0.19	133 ± 15	13.62	8.79	2.87
			0.46	0.71	2.18
CELL-C8-NTf$_2$	2.74 ± 0.24	216 ± 13	13.55	8.48	2.76
			0.46	0.74	2.27
CELL-C12-NTf$_2$	2.31 ± 0.18	252 ± 25	13.06	8.25	2.80
			0.48	0.76	2.24

[a]Scattering vectors (q_x) and calculated correlation lengths (d_x) for each observable peak from WAXS/SAXS combined X-ray scattering profiles are provided.

decrease in stress at break. Each film was tested in triplicate with data for each sample provided in Table 2.

X-ray scattering data was also acquired for all three dual-IL cellulosic materials **CELL-Cx-NTf$_2$**, an overlay of which is provided in Figure 3. WAXS/SAXS combined data analysis indicated that all three materials exhibit amorphous behavior as opposed to microcrystalline cellulose.[36,38] There are three distinct scattering peaks (q) present for all three materials. Correlation lengths were calculated from the scattering vector positions using the following equation:

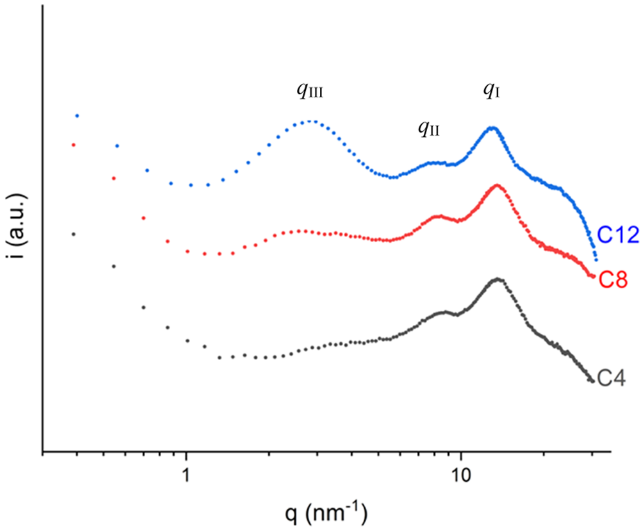

Figure 3. WAXS and SAXS combined X-ray scattering at 20 °C as a function of scattering vector (q) for the dual-IL-functionalized cellulosic materials.

$$d_x = 2\pi / q_x \tag{1}$$

where x refers to the specific type of correlation (I, II, or III), and the values are presented in Table 2. The high scattering vector, labeled as q_{I} (~10−11 nm^{-1}), is assigned to the amorphous halo and occurs due to various interactions between cation/anion pairs and the backbone which are separate from the neutral polymer. As all three cellulosic materials employ the same anion, very little change is observed between these signals and thus the correlation distances are nearly identical. This distance was also similar to our previously reported mono-IL-functionalized cellulosic materials.[36] The middle scattering vector, q_{II}, was attributed to the anion−anion distances with a calculated correlation distance of 0.71−0.76 nm. This distance was found to increase slightly with increasing alkyl chain spacer and was not present in scattering profiles for any of the **CELL-Cx-tri-im** or **CELL-Cx-Br** materials (Figures S52−S54). The lowest scattering vector, assigned q_{III} (~2.5−3.5 nm^{-1}), is assigned to the separation between aggregates and a correlation distance between 1.8 and 2.5 nm. The peak increases dramatically in intensity as the tether spacer changes from C4 to C12 since the increased spacing and hydrophobicity of the backbones lead to stronger, more isolated aggregates. A similar assignment of this low scattering peak to ion aggregation has been made in other poly(ionic liquid)s containing single pendant imidazolium groups with a variety of counteranions.[39,40] For example, Colby and co-workers reported a similar q vector at ~4 nm^{-1} for a series of imidazolium-containing poly(ionic liquid)s with different side chain lengths and either the [BF$_4$] or [NTf$_2$] counteranion.[40] They concluded that the intensity of this peak arises from the uniformity of the interaggregate spacing as well as electron density differences between the aggregates and the polymer matrix. Similarly, Segalman and co-workers observed that upon doping imidazole-functionalized polymers with certain salts, a new scattering vector was observed at $q \sim 2$−3 nm^{-1}.[25] As this vector did not shift to higher q upon increasing the salt concentration, they attributed this signal to the distance between domains of ion aggregates.

The conductivity of ion-containing polymers depends upon both the diffusion and concentration of ion species. A combination of other factors, many of which are difficult to separate, also contribute to conductivity, including T_g, polymer morphology and structure, and ion aggregation.[24,25,31,39−47] In the present work, ionic conductivity values were determined using the dielectric accessory of a rheometer under an atmosphere of dry nitrogen. Each sample was allowed to equilibrate at the desired temperature (130 to −10 °C in 10 °C steps) for 45 min prior to obtaining any data. As shown in Figure 4 (top), ionic conductivity was found to be on the order of 10^{-7}−10^{-6} S/cm at 30 °C. For reference, conductivity data for the previously reported mono-1,2,3-triazolium IL-substituted cellulose [NTf$_2$] material is also provided.

Comparing the curves in Figure 4 (top) of the three dual-IL cellulosic materials, the ionic conductivities of the **CELL-C8-NTf$_2$** and **CELL-C12-NTf$_2$** analogues were found to be parallel curves with the C8 derivative exhibiting a slightly higher conductivity, presumably due to its lower T_g-value. The conductivity curve for **CELL-C4-NTf$_2$** exhibited slightly different behavior. At lower temperatures, the C4 derivative was found to be the lowest conductor, but then, as temperature increased, the conductivity crossed over the C8 and C12 derivatives, resulting in the highest conductivity at elevated temperatures. The ionic conductivities were further plotted as a function of normalized T_g (Figure 4, bottom). Note that the C8 and C12 derivative curves effectively coalesce, emphasizing

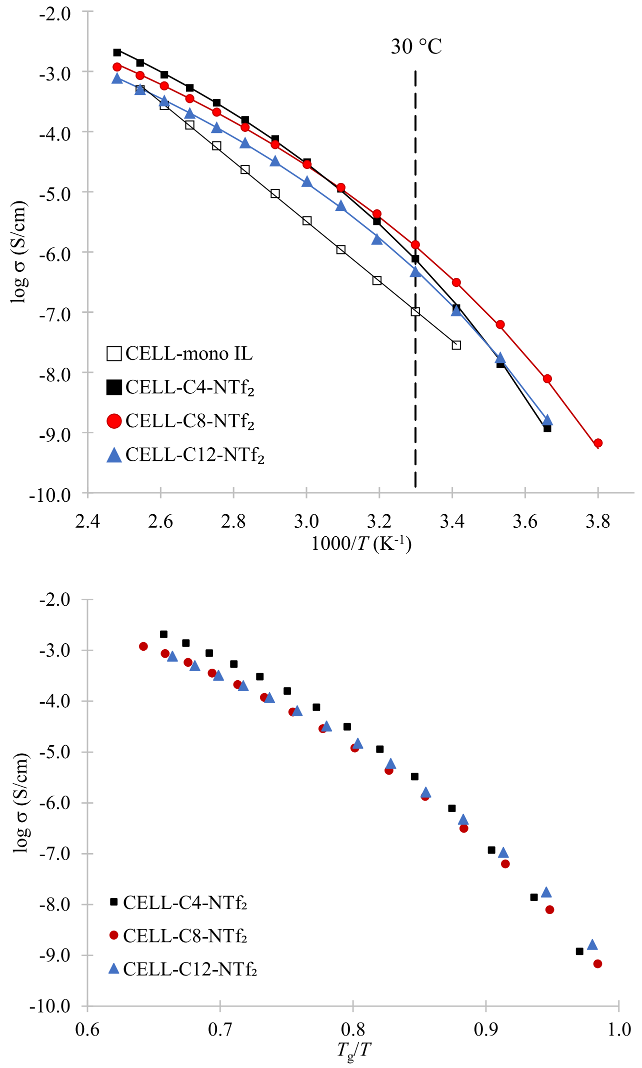

Figure 4. (Top) Ionic conductivity as a function of temperature for the dual-IL **CELL-Cx-NTf$_2$** series with Vogel−Fulcher−Tamman (VFT) fitting shown as solid curves. (Bottom) T_g-normalized conductivity curves.

that conductivity depends heavily on T_g. However, **CELL-C4-NTf$_2$** exhibits the highest T_g-normalized conductivity and does not coalesce well with the other data sets, especially at higher temperatures. As the three materials have a negligible difference in ion concentration and the polymer backbone (cellulose), and the degree of substitutions are essentially the same, ion aggregation is believed to be a major attribute in affecting ionic conductivity. We hypothesize that discrete aggregate clusters are formed in both **CELL-C12-NTf$_2$** and **CELL-C8-NTf$_2$**, resulting in electrostatic/Coulombic interactions that are more difficult to overcome, even at higher temperatures. The longer, hydrophobic alkyl chain lengths force the ions into clusters that are not interconnected, leading to poor ion hopping throughout the matrix. As **CELL-C4-NTf$_2$** utilizes the shortest tether, the counteranions are either not present in isolated clusters or the clusters must be interconnected (this distinction cannot be made with the present data), allowing for a greater increase in conductivity with temperature.

In comparison with the previously reported mono-IL cellulosic material, the inclusion of the second (imidazolium) IL group results in two noticeable changes in the conductivity data. First, the **CELL-Cx-NTf$_2$** materials exhibit conductivities which are approximately an order of magnitude higher than the mono-IL analogue across most of the same temperature range. Second, the **CELL-Cx-NTf$_2$** materials exhibit a nonlinear response to temperature unlike the linear (Arrhenius) behavior shown by the mono-IL analogue.[36] As all of the **CELL-Cx-NTf$_2$** materials exhibited T_g values below 0 °C, all of the conductivity data presented here were completed above the T_g, meaning that the dual IL-containing polymers rely on not only the "hopping" of free ions along the backbone of the polymer but also on other segmental motion and relaxation events of the polymer itself. This leads to a response that follows Vogel−Fulcher−Tamman (VFT) behavior as defined by the following equation:

$$\sigma(T) = \sigma_\infty \times \exp\left(\frac{-DT_o}{T - T_o}\right) \tag{2}$$

where σ_∞ is the infinite conductivity limit, D is the strength parameter, T_o is the Vogel temperature (the temperature at which ion mobility goes to zero and polymer relaxation time is infinite), and T is the experimental temperature.[27,47] VFT-fits for each of the **CELL-Cx-NTf$_2$** materials are provided as solid curves in Figure 4 (top) with fitting parameters provided in Table 3. High-temperature-limiting conductivity values (σ_∞) increase with decreasing alkyl tether length with **CELL-C4-NTf$_2$** exhibiting the highest value. As previously discussed, this system appears to have the least amount of ionic aggregation, meaning that, as the temperature increases, there must exist a higher degree of ion mobility. Other VFT fitting parameters, T_g−T_o and D (strength parameter) values, were found to be similar to other poly(ionic liquid)s, ionenes, and IL-containing networks reported in the literature with no discernible trend among the three derivatives.[27,41−44,47]

Table 3. VFT Fitting Parameters for CELL-Cx-NTf$_2$ Cellulosic Materials

material	σ at 30 °C (S/cm)	σ_∞ (S/cm)	D	T_g−T_o (K)
CELL-C4-NTf$_2$	7.75×10^{-7}	9.95	8.6	67
CELL-C8-NTf$_2$	1.32×10^{-6}	5.03	9.8	74
CELL-C12-NTf$_2$	5.98×10^{-7}	2.54	8.8	75

■ CONCLUSIONS

This paper demonstrates that microcrystalline cellulose can be modified utilizing azide−alkyne click cyclization to create flexible, conductive materials. In our prior work, we showed that the covalent attachment of a single 1,2,3-triazolium ionic liquid group effectively disrupted enough of the hydrogen-bonding interactions between cellulose chains that the material exhibited T_g values on the order of 90−100 °C depending on the counteranion used. Furthermore, X-ray scattering data indicated that the material was amorphous exhibiting ionic aggregates as a function of spacer length. This inspired us to expand on this idea to include an additional IL (imidazolium) unit onto each side chain with a variable tether between the two IL units, all while keeping the counteranion [NTf$_2$] the same. The additional IL unit resulted in several noticeable changes in thermal and mechanical properties. T_g values of the three **CELL-Cx-NTf$_2$** derivatives were all found to be below 0 °C with a dependency on the length of the alkyl chain tether length. An initial drop from C4 to C8 was observed, followed by a slight increase to C12, presumably due to intercalation of the longer side chains. Films of all three materials were cast from DMF and exhibited a significant increase in flexibility when compared to the mono-IL cellulosic materials. Stress and strain at break were found to be dependent on the length of the alkyl tether chain with an increase in chain length leading to a higher strain and break with only a slight decrease in stress at break.

X-ray scattering profiles confirmed the amorphous nature of all three **CELL-Cx-NTf$_2$** derivatives. Three scattering peaks were observed, from high-to-low q, corresponding to the amorphous halo, anion-to-anion distance, and the distance between ion aggregates, respectively. The highest degree of ionic aggregation was found to exist in the **CELL-C12-NTf$_2$** material, presumably due to the longer alkyl tethers causing more uniformity in the interaggregate spacing and greater electron density difference within the polymer matrix. Ion aggregation was also found to have an effect on ionic conductivity. **CELL-C8-NTf$_2$** and **CELL-C12-NTf$_2$** behaved similarly, while the C8 analogue exhibited a slightly higher conductivity. **CELL-C12-NTf$_2$** exhibited slightly different behavior in that its conductivity curve crossed over both the C8 and C12 analogues, with a lower conductivity at low temperatures and a higher conductivity at the highest temperatures. We hypothesize that stronger, more isolated ionic aggregations are observed in the C8 and C12 systems, leading to a slower increase in ionic conductivity with temperature as opposed to the C4 system where the aggregates are either more loosely held together or perhaps are more percolated throughout the matrix, leading to enhanced ion mobility with rising temperature. Overall, these results indicate that flexible, conductive materials with tunable thermal and mechanical properties can be readily prepared starting with sustainable biomaterials such as cellulose.

■ ASSOCIATED CONTENT

Supporting Information

The Supporting Information is available free of charge at https://pubs.acs.org/doi/10.1021/acsapm.3c02815.

Synthetic procedures for the C4 and C12 analogues, NMR (^{1}H, ^{13}C) and FTIR spectra of pertinent intermediates and final products, TGA and DSC data, and X-ray scattering overlays (PDF)

■ AUTHOR INFORMATION

Corresponding Author

Kevin M. Miller − *Department of Chemistry, Murray State University, Murray, Kentucky 42071, United States;* orcid.org/0000-0001-5314-7477; Email: kmiller38@murraystate.edu

Authors

Elizabeth A. Hays − *Department of Chemistry, Murray State University, Murray, Kentucky 42071, United States;* orcid.org/0009-0002-5250-9573

Gabrielle Eicher − *Department of Chemistry, Murray State University, Murray, Kentucky 42071, United States*

Abneris Morales − *Center for Computational and Integrative Biology, Rutgers University, Camden, New Jersey 08102, United States*

David Salas-de la Cruz − *Center for Computational and Integrative Biology, Rutgers University, Camden, New Jersey 08102, United States; Department of Chemistry, Rutgers University, Camden, New Jersey 08102, United States*

Complete contact information is available at: https://pubs.acs.org/10.1021/acsapm.3c02815

Notes

The authors declare no competing financial interest.

■ ACKNOWLEDGMENTS

Financial support was provided by the National Science Foundation under grant awards NSF-DMR (2104375 and 2104376) and NSF-CMMI (2037097). The DEXS System was supported by NSF-MRSEC 17-20530, NSF-MRI 17-25969, ARO DURIP W911NF-17-1-02822, and the University of Pennsylvania.

■ REFERENCES

(1) Klemm, D.; Heublein, B.; Fink, H.-P.; Bohn, A. Cellulose: Fascinating Biopolymer and Sustainable Raw Material. *Angew. Chem., Int. Ed.* **2005**, *44*, 3358−3393.

(2) Zheng, X. Y.; Gandour, R. D.; Edgar, K. J. TBAF-Catalyzed Deacetylation of Cellulose Esters: Reaction Scope and Influence of Reaction Parameters. *Carbohydr. Polym.* **2013**, *98*, 692−698.

(3) Tran, C. D.; Mututuvari, T. M. Cellulose, Chitosan and Keratin Composite Materials: Facile and Recyclable Synthesis, Conformation and Properties. *ACS Sustainable Chem. Eng.* **2016**, *4*, 1850−1861.

(4) Wu, J.; Yu, X.; Zhang, H.; Guo, J.; Hu, J.; Li, M. Fully Biobased Vitrimers from Glycyrrhizic Acid and Soybean Oil for Self-Healing, Shape Memory, Weldable, and Recyclable Materials. *ACS Sustainable Chem. Eng.* **2020**, *8*, 6479−6487.

(5) O'Dea, R. M.; Willie, J. A.; Epps, T. H., III 100th Anniversary of Macromolecular Science Viewpoint: Polymers from Lignocellulosic Biomass. Current Challenges and Future Opportuntities. *ACS Macro Lett.* **2020**, *9*, 476−493.

(6) Dalwadi, S.; Goel, A.; Kapetanakis, C.; Salas-de la Cruz, D.; Hu, X. The Integration of Biopolymer-Based Materials for Energy Storage Applications: A Review. *Int. J. Mol. Sci.* **2023**, *24*, 3975.

(7) Tarchoun, A. F.; Trache, D.; Klapötke, T. M.; Khimeche, K. J. C. E. J. Tetrazole-functionalized Microcrystalline Cellulose: A Promising Biopoymer for Advanced Energetic Materials. *Chem. Eng. J.* **2020**, *400*, No. 125960.

(8) Min, X.; Wu, T.; Han, X.; An, M.; Yu, W.; Li, L. Zero-zero Birefringence Cellulose Acetate-Based Optical Films by Benzoylation. *ACS Appl. Polym. Mater.* **2022**, *4*, 6255−6264.

(9) Tarrahi, R.; Khataee, A.; Karimi, A.; Yoon, Y. The Latest Achievements in Plant Cellulose-based Biomaterials for Tissue Engineering Focusing on Skin Repair. *Chemosphere* **2022**, *288*, No. 132529.

(10) Liebert, T.; Hansch, C.; Heinze, T. Click Chemistry with Polysaccharides. *Macromol. Rapid Commun.* **2006**, *27*, 208−213.

(11) Elchinger, P.-H.; Faugeras, P.-A.; Boens, B.; Brouillette, F.; Montplaisir, D.; Zerrouki, R.; Lucas, R. Polysaccharides: The "Click" Chemistry Impact. *Polymers* **2011**, *3*, 1607−1651.

(12) Baskin, J. M.; Prescher, J. A.; Laughlin, S. T.; Agard, N. J.; Chang, P. V.; Miller, I. A.; Lo, A.; Codelli, J. A.; Bertozzi, C. R. Copper-Free Click Chemistry for Dynamic *in vivo* Imaging. *Proc. Natl. Acad. Sci. U.S.A.* **2007**, *104*, 16793−16797.

(13) Sun, L.; Xiao, G.; Qian, X.; An, X. Alkyne Functionalized Cellulose Fibers: A Versatile "Clickable" Platform for Antibacterial Materials. *Carbohydr. Polym.* **2019**, *207*, 68−78.

(14) Yuan, J.; Mecerreyes, D.; Antonietti, M. Poly(ionic liquid)s: an update. *Prog. Polym. Sci.* **2013**, *38*, 1009−1036.

(15) Qian, W.; Texter, J.; Yan, F. Frontiers in poly(ionic liquid)s: syntheses and applications. *Chem. Soc. Rev.* **2017**, *46*, 1124−1159.

(16) Biswas, Y.; Banerjee, P.; Mandal, T. K. From Polymerized Ionic Liquids to Poly(ionic liquid)s: Structure-Dependent Thermal, Crystalline, Conductivity, and Solution Thermoresponsive Behaviors. *Macromolecules* **2019**, *52*, 945−958.

(17) Shaplov, A. S.; Marcilla, R.; Mecerreyes, D. Recent advances in innovative polymer electrolytes based on poly(ionic liquid)s. *Electrochim. Acta* **2015**, *175*, 18−34.

(18) Miao, L.; Song, Z.; Zhu, D.; Li, L.; Gan, L.; Liu, M. Ionic liquids for supercapacitive energy storage: A mini-review. *Energy Fuels* **2021**, *35*, 8443−8455.

(19) Cowan, M. G.; Gin, D. L.; Noble, R. D. Poly(ionic liquid)/ ionic liquid ion-gels with high "free" ionic liquid content: Platform membrane materials for CO_2/light gas separations. *Acc. Chem. Res.* **2016**, *49*, 724−732.

(20) Gao, J.; Zhang, Y.; Son, J.; Bara, J. E.; O'Harra, K. E.; Engelhard, M. H.; Heldebrant, D. J.; Rousseau, R.; Yu, X.-Y. The interfacial compatibility between a potential CO_2 separation membrane and capture solvents. *Carbon Capture Sci. Technol.* **2022**, *2*, No. 100037.

(21) Klein, R. J.; Zhang, S.; Dou, S.; Jones, B. H.; Colby, R. H.; Runt, J. Modeling electrode polarization in dielectric spectroscopy: Ion mobility and mobile ion concentration of single-ion polymer electrolytes. *J. Chem. Phys.* **2006**, *124*, No. 144903.

(22) Zhao, J.; Lei, Q.; He, F.; Zheng, C.; Liu, Y.; Zhao, X.; Yin, J. Interfacial polarization and electroresponsive effect of anionic and cationic poly(ionic liquid)s. *ACS Appl. Polym. Mater.* **2019**, *1*, 2862−2874.

(23) Choi, U. H.; Ye, Y.; Salas-de la Cruz, D.; Liu, W.; Winey, K. I.; Elabd, Y. A.; Runt, J.; Colby, R. H. Dielectric and Viscoelastic Responses of Imidazolium-Based Ionomers with Different Counterions and Side Chain Lengths. *Macromolecules* **2014**, *47*, 777−790.

(24) Wheatle, B. K.; Lynd, N. A.; Genesan, V. Effect of Polymer Polarity on Ion Transport: A Competition between Ion Aggregation and Polymer Segmental Dynamics. *ACS Macro Lett.* **2018**, *7*, 1149−1154.

(25) Schauser, N. S.; Grzetic, D. J.; Tabassum, T.; Kliegle, G. A.; Le, M. L.; Susca, E. M.; Antoine, S.; Keller, T. J.; Delaney, K. T.; Han, S.; Seshardi, R.; Fredrickson, G. H.; Segalman, R. A. The Role of Backbone Polarity on Aggregation and Conduction of Ions in Polymer Electrolytes. *J. Am. Chem. Soc.* **2020**, *142*, 7055−7065.

(26) Iacob, C.; Matsumoto, A.; Brennan, M.; Liu, H.; Paddison, S. J.; Urakawa, O.; Inoue, T.; Sangoro, J.; Runt, J. Polymerized Ionic Liquids: Correlation of Ionic Conductivity with Nanoscale Morphology and Counterion Volume. *ACS Macro Lett.* **2017**, *6*, 941−946.

(27) Bontrager, N. C.; Radomski, S.; Daymon, S. P.; Johnson, R. D.; Miller, K. M. Influence of Counteranion and Humidity on the Thermal, Mechanical, and Conductive Properties of Covalently Crosslinked Ionenes. *Polymer* **2021**, *222*, No. 123641.

(28) Obadia, M. M.; Drockenmuller, E. Poly(1,2,3-triazolium)s: A New Class of Functional Polymer Electrolytes. *Chem. Commun.* **2016**, *52*, 2433−2450.

(29) Obadia, M. M.; Jouradin, A.; Cassagnau, P.; Montarnal, D.; Drockenmuller, E. Tuning the viscosity profile of ionic vitrimers incorporating 1,2,3-triazoloium cross-links. *Adv. Funct. Mater.* **2017**, *27*, No. 1703258.

(30) Jourdain, A.; Asbai, R.; Anaya, O.; Chehimi, M. M.; Drockenmuller, E.; Montarnal, D. Rheological properties of covalent adaptable networks with 1,2,3-triazolium cross-links: The missing link between vitrimers and dissociative networks. *Macromolecules* **2020**, *53*, 1884−1900.

(31) Tracy, C. A.; Adler, A. M.; Nguyen, A.; Johnson, R. D.; Miller, K. M. Covalently Crosslinked 1,2,3-Triazolium-Containing Polyester Networks: Thermal, Mechanical and Conductive Properties. *ACS Omega* **2018**, *3*, 13442−13453.

(32) Chen, Q.; Peng, C.; Xie, H.; Zhao, Z. K.; Bao, M. Cellulosic poly(ionic liquid)s: Synthesis, characterization and application of CO2 to epoxides. *RSC Adv.* **2015**, *5*, 44598−44603.

(33) Bernard, F. L.; Duczinski, R. B.; Rojas, M. F.; Fialho, M. C. C.; Carreno, L. A.; Chaban, V. V.; Vecchia, F. D.; Einloft, S. Cellulose based poly(ionic liquid)s: Tuning cation-anion interaction to improve carbon dioxide sorption. *Fuel* **2018**, *211*, 76−86.

(34) Singh, A.; Singh, N.; Kaur, N.; Jang, D. O. Gold nanoparticles supported on ionic-liquid-functionalized cellulose (Au@CIL): A heterogeneous catalyst for the selective reduction of aromatic nitro compounds. *Appl. Organomet. Chem.* **2022**, *36*, No. e6855.

(35) Tan, W.; Li, Q.; Gao, Z.; Qiu, S.; Dong, F.; Guo, Z. Design, synthesis of novel starch derivative bearing 1,2,3-triazolium and pyridinium and evaluation of its antifungal activity. *Carbohydr. Polym.* **2017**, *157*, 236−243.

(36) Miller, R. J.; Smith, V. M.; Love, S. A.; Byron, S. M.; Salas-de la Cruz, D.; Miller, K. M. Synthesis and Evaluation of Cellulose-based, 1,2,3-Triazolium-functionalized Polymerized Ionic Liquids: Thermal Transitions, Ionic Conductivities, and Morphological Properties. *ACS Appl. Polym. Mater.* **2021**, *3*, 1097−1106.

(37) Scammells, P. J.; Scott, J. L.; Singer, R. D. Ionic Liquids: The Neglected Issues. *Aust. J. Chem.* **2005**, *58*, 155−169.

(38) Ganesan, V.; Pyramitsyn, V.; Bertoni, C.; Shah, M. Mechanisms Underlying Ion Transport in Lamellar Block Copolymer Membranes. *ACS Macro Lett.* **2012**, *1*, 513−518.

(39) Cui, J.; Nie, F.; Yang, J.; Pan, L.; Ma, Z.; Li, Y. Novel Imidazolium-based Poly(ionic liquid)s with Different Counterions for Self-Healing. *J. Mater. Chem. A* **2017**, *5*, 25220−25229.

(40) Choi, U. H.; Ye, Y.; Salas-de la Cruz, D.; Liu, W.; Winey, K. I.; Elabd, Y. A.; Runt, J.; Colby, R. H. Dielectric and Viscoelastic Ionomers with Different Counternions and Side Chain Lengths. *Macromolecules* **2014**, *47*, 777−790.

(41) Stacy, E. W.; Gainaru, C. P.; Gobert, M.; Wojnarowska, Z.; Bocharova, V.; Greenbaum, S. G.; Sokolov, A. P. Fundamental Limitations of Ionic Conductivity in Polymerized Ionic Liquids. *Macromolecules* **2018**, *51*, 8637−8645.

(42) Zardalidis, G.; Pipertzis, A.; Mountrichas, G.; Pispas, S.; Mezger, M.; Loudas, G. Effect of Polymer Architecture on the Ionic Conductivity. Densely Grafted Poly(ethylene oxide) Brushes Doped with LiTf. *Macromolecules* **2016**, *49*, 2679−2687.

(43) Evans, C. M.; Bridges, C. R.; Sanoja, G. E.; Bartels, J.; Segalman, R. A. Role of Tetherd Ion Placement on Polymerized Ionic Liquid Structure and Conductivity: Pendant versus Backbone Charge Placement. *ACS Macro Lett.* **2016**, *5*, 925−930.

(44) Hall, L. M.; Stevens, M. J.; Frischknecht, M. L. Effect of Polymer Architecture and Ionic Aggregation on the Scattering Peak in Model Ionomers. *Phys. Rev. Lett.* **2011**, *106*, No. 127801.

(45) Abbott, L. J.; Lawson, J. W. Effects of Side Chain Length on Ionic Aggregation and Dynamics in Polymer Single-Ion Conductors. *Macromolecules* **2019**, *52*, 7456.

(46) Keith, J. R.; Rebello, N. J.; Cowen, B. J.; Ganesan, V. Polymerized ionic liquids: Correlation of ionic conductivity with nanoscale morphology and counteranion volume. *ACS Macro Lett.* **2019**, *8*, 387−392.

(47) Rhoades, T. C.; Wistrom, J. C.; Johnson, R. D.; Miller, K. M. Thermal, mechanical, and conductive properties of imidazolium-containing thiol-ene poly(ionic liquid)s. *Polymer* **2016**, *100*, 1−9.

https://doi.org/10.1021/acsapm.3c02815